

Imaging the potential distribution of charged adsorbates on graphene by low-energy electron holography

Tatiana Latychevskaia*, Flavio Wicki, Conrad Escher, Hans-Werner Fink

Physics Department, University of Zurich,

Winterthurerstrasse 190, 8057 Zurich, Switzerland

*Corresponding author: tatiana@physik.uzh.ch

ABSTRACT

While imaging individual atoms can routinely be achieved in high resolution transmission electron microscopy, visualizing the potential distribution of individually charged adsorbates leading to a phase shift of the probing electron wave is still a challenging task. Since low-energy electrons are sensitive to localized potential gradients, we employed this tool in the 30 eV kinetic energy range to visualize the potential distribution of localized charged adsorbates present on free-standing graphene.

PACS: 81.05.ue, 73.22.Pr, 68.37.Nq, 07.78+s, 61.05.jp

I. INTRODUCTION

The charge density, respectively the electrostatic potential of atoms in crystals can directly be probed by x-ray [1-2] or electron [3-5] scattering. However, such diffraction experiments are limited to crystals, and the challenging task is to visualize the charge density or electrostatic potential of an individual adsorbate. Recently, by combining techniques such as high-resolution transmission electron microscopy with first-principles electronic structure calculations [6] or scanning tunneling microscopy with Raman spectroscopy, or x-ray spectroscopy with first principles calculations [7] it has been demonstrated that the charge redistribution due to chemical bonding of nitrogen dopants to graphene could be revealed.

Calculations based on the Density Functional Theory (DFT) show that most adatoms transfer electrons to graphene [8], initiating a charge redistribution in their vicinity. It has recently been suggested that charged impurities are the predominant source of disorder in most graphene samples leading to a limited charge carrier mobility [9], vital for graphene applications in mesoscopic devices.

Recently, we reported that individual charged adsorbates on graphene provide sufficient contrast to be detected by low-energy electron holography [10]. The principle of low-energy electron holography is schematically illustrated in Fig. 1(a): the electron wave passes through the free-standing graphene sample while part of the wave is scattered by the object. Interference between the scattered and non-scattered wave leads to a hologram recorded at a distant detector. Various processes are conceivable when a low-energy electron is interacting with the sample [11]. Firstly, an incident electron can be elastically scattered by a localized potential within the sample. In fact, the scattering for low-energy electrons exhibits pronounced maxima of the scattering amplitude in forward and backward directions [12]. Moreover, electron energy losses due to excitations of phonons or plasmons are conceivable as well as absorption of electrons. The final distribution of the object wave respectively its signature at the detector is the time-average over these two main processes, forward scattering and absorption.

Theoretical simulations for electron scattering and absorption by an individual atom on graphene are complicated if not impossible to perform. The phase shifts that form the scattering amplitude expansion are conventionally obtained for a certain model of the scattering potential [12]. The later in turn should be built by taking into account the electron distribution of the atom. The task becomes particularly difficult when the atom is charged, leading to re-distribution of electrons within the atom. Here, we would like to cite John Pendry: “The ion-core potential acts on conducting electrons influencing their motion, and therefore changes their charge density. The problem is a self-consistent one and indeed when

accurate band structure calculations are needed an iterative procedure for calculating ion-core scattering conduction electron density, and the ion core scattering again with the new screening charge, must be employed: a tedious procedure” [11]. And even if such potential of a charged atom would be available, it would be again only a rough approximation. A correct model must take the graphene support into account with all its imperfections such as adsorbates, vacancies etc. The potential distribution associated with an individual charged atom appears therefore impossible to accurately predict by theory. We show how projected potentials of individual charged adsorbates can be measured from experimental low-energy electron holograms.

II. EXPERIMENTAL SETUP

A typical setup for low-energy electron holography [13] is depicted in Fig. 1 and explained in detail in [10, 14]; graphene samples were prepared as described elsewhere [15]. Electrons are field emitted from a sharp tungsten tip. Since transparent free-standing graphene provides an overall equipotential plane, a neutral adsorbate present on graphene results in an ordinary hologram, as illustrated in Fig. 1(b). However, a charged adsorbate locally creates a high electric field deflecting the passing electrons. The presence of a charged adsorbate thus leads to a distinctive signature in the hologram, a bright spot, as illustrated in Fig. 1(c).

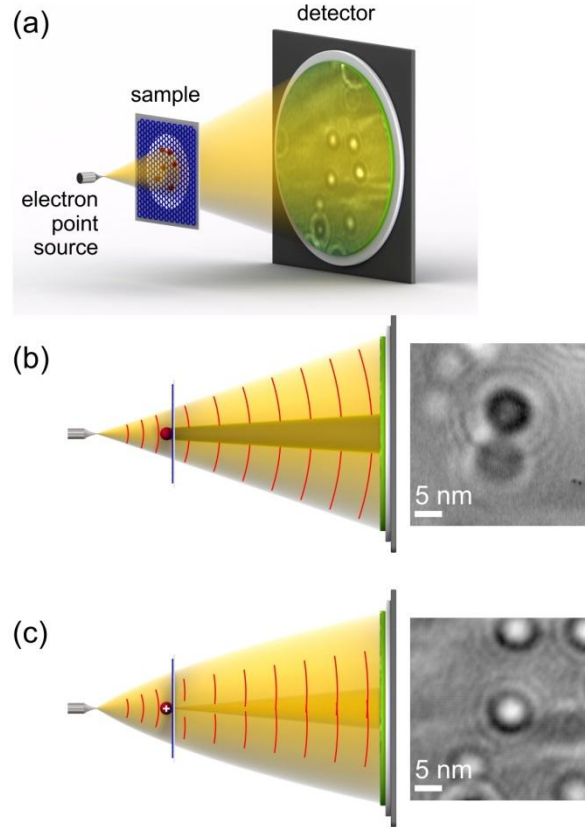


FIG. 1. Experimental arrangement. (a) Low-energy electron holographic microscope. The distance from source to sample is in the range of tens of nanometres and the distance from source to detector amounts to 47 mm. (b) Imaging of a neutral adsorbate whereby part of the beam is absorbed resulting in an ordinary hologram. (c) Imaging of a positively charged adsorbate. The electron trajectories are deflected inward by the presence of a positive charge resulting in a bright spot on the detector.

III. EXPERIMENTAL RESULTS

Apart from the interference patterns typical for neutral adsorbates, we also observe particularly bright spots. The hologram reconstruction of the latter however becomes more involved.

To begin with, the reconstruction procedure was carried out for different source-to-sample distances ranging from 10 nm to 1000 nm. At a source-to-sample distance of 82 nm, objects such as clusters appear in focus; hence, this distance was identified as the correct source-to-sample distance. However, in the reconstruction that we obtained, the bright spots did not converge to a meaningful object reconstruction. As demonstrated previously [10], such bright spots are ascribable to positively charged adsorbates. Since a charged adsorbate deflects even those electrons which are passing the charged adsorbate at some distance, the reference wave is destroyed. Consequently, the lack of a well defined reference wave precludes ordinary reconstruction of the holograms. The problem of object reconstruction from such interference pattern is equivalent to the phase retrieval problem in coherent diffraction imaging, where only the intensity of the scattered wave is detected but no reference wave is present [16].

Four such bright spots are shown in Fig. 2(a), they are all located within one sample, and the distances between the charged adsorbates vary from 11.6 to 20.6 nm. Each bright spot was reconstructed separately by applying an iterative procedure as explained in Appendix I. The iteratively fitted intensity distributions are shown in Fig. 2(b). The error of the fitted intensity is evaluated as following:

$$E = \frac{1}{N^2} \sum_{i,j=1}^N \left| \frac{I_{\text{measured}}(i, j) - I_{\text{iterated}}(i, j)}{I_{\text{measured}}(i, j)} \right|, \quad (1)$$

which is an estimate of the difference between the measured and the iterated values in relation to the measured values and averaged over all pixels. The errors estimated for the four spots are small: $E_1 = 0.07\%$, $E_2 = 0.08\%$, $E_3 = 0.09\%$ and $E_4 = 0.09\%$. The radial profiles of the measured and the iteratively fitted intensity distributions are in good congruence as shown in Fig. 2(c).

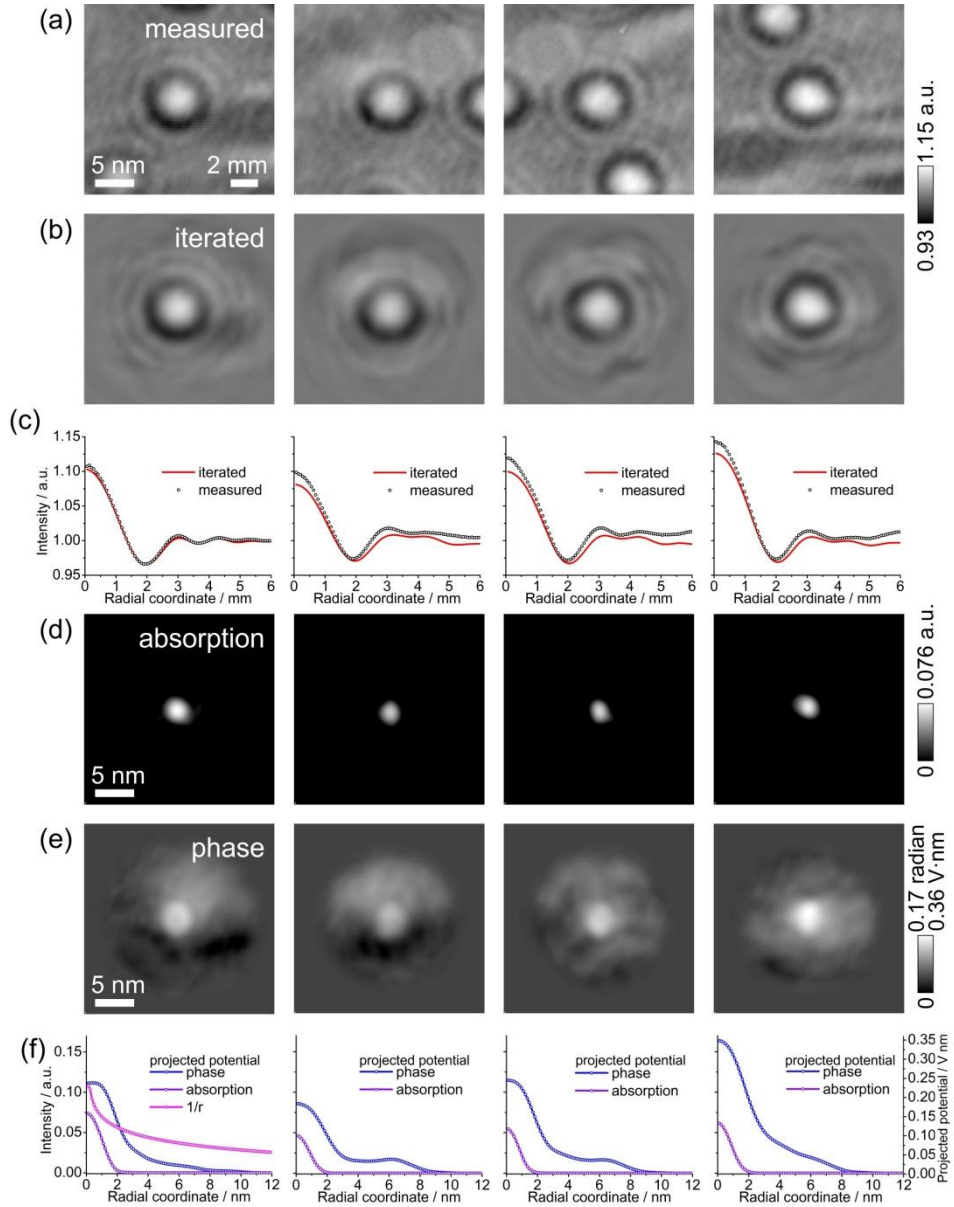


FIG. 2. Iteratively reconstructed absorption and phase distribution of charged adsorbates. (a) Four selected bright spots in a hologram acquired with electrons of 30 eV kinetic energy. (b) The related intensity distributions obtained after 2000 iterations. (c) The radial profiles of the measured and iteratively obtained intensity distributions. (d) and (e) The related absorption and phase distributions and (f) their radial profiles.

IV. DISCUSSION

Figure 2 shows reconstructed absorption and phase distributions. The full width at half maximum (FWHM) for the four adsorbates shown in Fig. 2 amounts to: $\text{FWHM}_1 = 2.1 \text{ nm}$, $\text{FWHM}_2 = 1.5 \text{ nm}$, $\text{FWHM}_3 = 1.5 \text{ nm}$ and $\text{FWHM}_4 = 1.9 \text{ nm}$. These values are relatively large when comparing them to the empiric covalent radii of typical adsorbates found on graphene: 70 pm for carbon, 25 pm for hydrogen, 60 pm for oxygen and 110 pm for silicon [17]. The discrepancy can be explained by the limited resolution of the low-energy electron holographic setup. The intrinsic resolution of the setup is defined by the formula:

$$R_{\text{intrinsic}} = \frac{\lambda}{2\text{NA}}, \quad (2)$$

where NA is the numerical aperture of the setup. The intrinsic resolution of the setup with a detector diameter of 75 mm at the wavelength of 0.22 nm for 30 eV electrons amounts to

$$R_{\text{intrinsic}} = \frac{\lambda}{2\text{NA}} = 0.23 \text{ nm}. \text{ However, the resolution is degraded by residual mechanical}$$

vibrations smearing the fine interference fringes in the hologram thus leading to the decrease of the effective size of the hologram, which in turn leads to a blurry appearance of the reconstructions. Moreover, the fact that the reference wave does not coherently illuminate the entire detector, also contributes to a limited experimental resolution. The maxima of the retrieved absorption distributions are relatively small: $a_1 = 0.08$, $a_2 = 0.05$, $a_3 = 0.06$ and $a_4 = 0.07$. When the adsorbate is not charged, the effect of absorption alone results in a hologram which exhibits a very weak contrast not distinguishable from the noise level.

As evident from the reconstructions shown in Fig. 2, the reconstructed absorption distributions (Fig. 2(d)) appear to be narrower than the reconstructed phase distributions (Fig. 2(e)). This agrees well with the notion that the phase distribution unlike the absorption distribution does not reflect actual size of the adsorbate itself but rather its potential distribution caused by the charge.

The reconstructed phase shift distribution $\Delta\varphi(x, y)$ can be interpreted as a projected potential [18], see Appendix II:

$$\Delta\varphi(x, y) = \frac{2\pi e}{h\nu} V_{\text{proj}}(x, y), \quad (3)$$

where e is the elementary charge, h is the Planck's constant, $\nu = \sqrt{2eU/m_e}$ is the speed of the probing electrons, U is the accelerating voltage, m_e is the electron mass and $V_{\text{proj}}(x, y)$ is denoting the projected electrostatic potential:

$$V_{\text{proj}}(x, y) = \int_{\text{path}} V(x, y, z) dz, \quad (4)$$

where $V(x, y, z)$ is the electrostatic potential along the path of the probing electrons.

From the phase distributions shown in Fig. 2 it is evident that the potential of a charged adsorbate is almost constant within the area occupied by the adsorbate, reaching about $(V_{\text{proj}})_{\text{max}} = 0.25 - 0.35 \text{ V} \cdot \text{nm}$. The potential quickly decays outwards towards 0 within 9 – 10 nm distance from the adsorbate. For comparison, we used a potential of the form $V(r) = 0.035e/r$ to simulate the corresponding projected potential. The radial distribution of the simulated projected potential is shown in Fig. 2(f) (first panel on the left). It exhibits no fast decay when compared to the experimentally obtained projected potential and does not reach zero. Thus, the realistic potential distribution can only roughly be approximated by a $1/r$ dependency [10] that corresponds to a free charge and disregards any shielding due to electronic rearrangement within the substrate.

CONCLUSIONS

We demonstrated how projected potentials of individual adsorbates can be obtained from their low-energy electron holograms. The projected potential amounts to 0.25 – 0.35 V·nm. It displays a rapid decay towards zero within a distance of 9-10 nm from the adsorbate.

APPENIX I

The iterative reconstruction procedure applied here is based on the procedure described elsewhere [19-20]. The reconstruction starts in the hologram plane. (i) The hologram is reconstructed and the transmission function in the object plane $t(x, y)$ is extracted using an algorithm for hologram reconstruction described elsewhere [21-22]. The transmission function in the object plane is given by $t(x, y) = \exp[-a(x, y)] \exp[-i\varphi(x, y)]$, where $a(x, y)$ denotes the absorption and $\varphi(x, y)$ the phase distributions respectively. (ii) In the object plane the following constraint is applied: $a(x, y) \geq 0$ based on a physical notion that the absorption cannot be negative [19]. Next, negative values of $a(x, y)$ are thus replaced with zeros, and an updated $a'(x, y)$ is obtained in this way. No constraint is imposed on the phase distribution $\varphi(x, y)$. (iii) Next, the wavefront distribution in the detector plane is simulated with the updated transmission function $t(x, y) = \exp[-a'(x, y)] \exp[-i\varphi(x, y)]$ [22]. (iv) The amplitude of the simulated wavefront is replaced with the measured amplitude given by the square root of the measured hologram intensity. The phase distribution of the simulated wavefront is adapted for the next iteration starting at (i). 2000 iterations were applied in total. The recovered absorption distribution was smoothed to avoid accumulation of noisy peaks. During the first 1000 iterations, the absorption distribution starts to form a pronounced peak with a width of about 2 nm. For the remaining 1000 iterations a loose

support of 5 nm in radius was applied to suppress artefacts around the absorption reconstruction.

APPENIX II

A plane wave impinging onto an object with the electric potential V and/or a magnetic potential \vec{A} experiences a phase modulation. To obtain the phase of the exit wave, the so-called eikonal equation along all possible trajectories is evaluated:

$$\varphi_{\text{obj}} = 2\pi \int_{\text{path}} \vec{k}_{\text{obj}} \cdot d\vec{s}, \quad (5)$$

where

$$\vec{k}_{\text{obj}} = \frac{\sqrt{2em(U+V)}}{h} \vec{e}_p - \frac{e}{h} \vec{A}, \quad (6)$$

with \vec{e}_p being the unit vector along the trajectory. In the absence of the object, we obtain:

$$\varphi_{\text{vac}} = 2\pi \int_{\text{vac}} \vec{k}_0 \cdot d\vec{s}, \quad (7)$$

where

$$\vec{k}_0 = \frac{\sqrt{2em_e U}}{h} \vec{e}_p. \quad (8)$$

Here e is the elementary charge, h is the Planck's constant, $v = \sqrt{2eU/m_e}$ is the speed of the probing electrons, U is the accelerating voltage and m_e is the electron mass.

The phase shift due to the electrostatic potential V when comparing it to the vacuum is thus given by

$$\begin{aligned}\Delta\varphi_{\text{obj}} &= 2\pi \int_{\text{path}} \left(\frac{\sqrt{2em_e(U+V)}}{h} - \frac{\sqrt{2em_eU}}{h} \right) ds = \\ &= 2\pi \frac{\sqrt{2em_eU}}{h} \int_{\text{path}} \left(\sqrt{\frac{U+V}{U}} - 1 \right) ds \approx 2\pi \frac{e}{\hbar v} \int_{\text{path}} V ds,\end{aligned}\tag{9}$$

where we applied the approximation $U \gg V$ and introduced $v = \sqrt{2eU/m_e}$ as the speed of the probing electrons.

REFERENCES

1. P. Coppens, and E. D. Stevens, "Accurate X-ray diffraction and quantum chemistry: the study of charge density distributions," *Advances in Quantum Chemistry* **10**, 1–35 (1977).
2. T. S. Koritsanszky, and P. Coppens, "Chemical applications of X-ray charge-density analysis," *Chem. Rev.* **101**, 1583–1627 (2001).
3. G. Radi, "Complex lattice potentials in electron diffraction calculated for a number of crystals," *Acta Crystallographica Section a-Crystal Physics Diffraction Theoretical and General Crystallography* **A 26**, 41-56 (1970).
4. M. Gajdardziskajosifovska, M. R. McCartney, W. J. Deruijter, D. J. Smith, J. K. Weiss, and J. M. Zuo, "Accurate measurements of mean inner potential of crystal wedges using digital electron holograms," *Ultramicroscopy* **50**, 285–299 (1993).
5. J. M. Zuo, "Measurements of electron densities in solids: a real-space view of electronic structure and bonding in inorganic crystals," *Rep. Prog. Phys.* **67**, 2053–2103 (2004).
6. J. C. Meyer, S. Kurasch, H. J. Park, V. Skakalova, D. Kunzel, A. Gross, A. Chuvilin, G. Algara-Siller, S. Roth, T. Iwasaki, U. Starke, J. H. Smet, and U. Kaiser, "Experimental analysis of charge redistribution due to chemical bonding by high-resolution transmission electron microscopy," *Nature Mater.* **10**, 209–215 (2011).
7. L. Y. Zhao, R. He, K. T. Rim, T. Schiros, K. S. Kim, H. Zhou, C. Gutierrez, S. P. Chockalingam, C. J. Arguello, L. Palova, D. Nordlund, M. S. Hybertsen, D. R. Reichman, T. F. Heinz, P. Kim, A. Pinczuk, G. W. Flynn, and A. N. Pasupathy, "Visualizing individual Nitrogen dopants in monolayer graphene," *Science* **333**, 999–1003 (2011).
8. X. J. Liu, C. Z. Wang, M. Hupalo, H. Q. Lin, K. M. Ho, and M. C. Tringides, "Metals on graphene: interactions, growth morphology, and thermal stability," *Crystals* **3**, 79–111 (2013).
9. Z. Fan, A. Uppstu, and A. Harju, "Dominant source of disorder in graphene: Charged impurities or ripples?," arXiv, 1605.03715 (2016).
10. T. Latychevskaia, F. Wicki, J.-N. Longchamp, C. Escher, and H.-W. Fink, "Direct observation of individual charges and their dynamics on graphene by low-energy electron holography," *Nano Lett.* **16**, 5469–5474 (2016).
11. J. B. Pendry, *Low-energy electron diffraction* (Academic Press London and New York, 1974).

12. NIST, *NIST electron elastic-scattering cross-section database* (2000).
13. H.-W. Fink, W. Stocker, and H. Schmid, "Holography with low-energy electrons," *Phys. Rev. Lett.* **65**, 1204–1206 (1990).
14. F. Wicki, J.-N. Longchamp, T. Latychevskaia, C. Escher, and H.-W. Fink, "Mapping unoccupied electronic states of freestanding graphene by angle-resolved low-energy electron transmission," *Phys. Rev. B* **94**, 075424 (2016).
15. J.-N. Longchamp, C. Escher, and H.-W. Fink, "Ultraclean freestanding graphene by platinum-metal catalysis," *J. Vac. Sci. Technol. B* **31**, 020605 (2013).
16. J. W. Miao, P. Charalambous, J. Kirz, and D. Sayre, "Extending the methodology of X-ray crystallography to allow imaging of micrometre-sized non-crystalline specimens," *Nature* **400**, 342–344 (1999).
17. J. C. Slater, "Atomic radii in crystals," *Journal of Chemical Physics* **41**, 3199 – 3205 (1964).
18. H. Lichte, and M. Lehmann, "Electron holography – basics and applications," *Rep. Prog. Phys.* **71**, 1–46 (2008).
19. T. Latychevskaia, and H.-W. Fink, "Solution to the twin image problem in holography," *Phys. Rev. Lett.* **98**, 233901 (2007).
20. T. Latychevskaia, P. Formanek, C. T. Koch, and A. Lubk, "Off-axis and inline electron holography: Experimental comparison," *Ultramicroscopy* **110**, 472–482 (2010).
21. T. Latychevskaia, J.-N. Longchamp, and H.-W. Fink, "When holography meets coherent diffraction imaging " *Opt. Express* **20**, 28871–28892 (2012).
22. T. Latychevskaia, and H.-W. Fink, "Practical algorithms for simulation and reconstruction of digital in-line holograms," *Appl. Optics* **54**, 2424–2434 (2015).